AIAA JOURNAL
Vol. 45, No. 7, July 2007

Attenuation of Low-Speed Flow-Induced Cavity Tones Using Plasma Actuators

Sammie Chan,* Xin Zhang,† and Steve Gabriel‡
University of Southampton, Southampton, SO17 1BJ England, United Kingdom

DOI: 10.2514/1.26645

The aeroacoustic environment of an open cavity with a length-to-depth (L/D) ratio of 1.0 was studied with and without plasma actuators. The study was conducted through low-speed wind-tunnel experiments at freestream velocities between 10 and 20 m/s, corresponding to Reynolds numbers based on the depth of the cavity of 3.6×10^4 to 7.1×10^4. The fluid flow inside the cavity was studied using a range of measurement techniques, which include oil flow, particle imaging velocimetry, and surface-mounted-microphone measurements. For acoustic control, an array of plasma actuators were located on the approaching surface to the cavity, aligned with the direction of the oncoming flow. Results show that the plasma actuators lead to a significant attenuation of the dominant cavity mode. The particle imaging velocimetry surveys around the electrode elements reveal vortical structures produced by the plasma actuators. These structures convect downstream with the mean flow and produce spanwise variations in the flow over the cavity that affect the spanwise coherence of the shear layer and hence the corresponding Rossiter mode.

Nomenclature

a	=	Rossiter mode
C_p	=	pressure coefficient, $(p - p_\infty)/\frac{1}{2}\rho_\infty U_\infty^2$
c	=	speed of sound
D	=	cavity depth
d_y	=	vertical distance
d_z	=	spanwise distance
f	=	audio frequency
H	=	shape factor, δ^*/θ
h	=	wind-tunnel test-section height
I	=	electrical current
K	=	dielectric constant
L	=	cavity length
M	=	Mach number
n	=	duct mode
St	=	Strouhal number, fD/U_∞
U_∞	=	freestream velocity
u, v, w	=	velocity components in Cartesian coordinates
$u_{i\text{-max}}$	=	maximum plasma-actuator-induced velocity
V_{dc}	=	dc voltage
V_{pp}	=	peak-to-peak voltage
x, y, z	=	Cartesian coordinates
α	=	feedback-oscillation lag factor
γ	=	ratio of specific heats
δ	=	boundary-layer thickness
δ_Ω	=	vorticity thickness
δ^*	=	displacement thickness
θ	=	momentum thickness
κ	=	ratio of convective velocity of disturbances to freestream velocity
ν_0	=	plasma operating frequency
Ω	=	vorticity
$\langle\,\rangle$	=	time-averaged quantity

Subscripts

$()_{duct}$	=	corresponding to the duct mode
$()_{exp}$	=	experimental value
$()_{lower}$	=	corresponding to the minimum u component
$()_{theory}$	=	theoretical value
$()_{upper}$	=	corresponding to the maximum u component
$()_x$	=	corresponding to the x value
$()_z$	=	corresponding to the z value

I. Introduction

THE popularity and dramatic rise in air travel in recent years has led to an increase in air traffic and drawn the attention of communities that live near airports, in regard to noise pollution. The development of aeroengines with high-bypass-ratio ducts and sound-absorbing materials has been the main contributor of aircraft noise moving from the engines to the airframe during the landing phase [1,2]. This includes high-lift devices, landing gear, and landing-gear bays that resemble large cavities. Airframe noise is particularly evident in the landing configuration when the engines are at a low power setting with the high-lift devices and landing gear deployed. Flying at close proximity to local communities for long periods of time in the landing configuration has led to legislation and monitoring of these noise levels exposed to the community. The environmental targets set by the Advisory Council for Aeronautics Research in Europe (ACARE) in their Strategic Research Agenda include a reduction of perceived noise level of 50% by 2020 [3,4]. More important, a quieter aircraft holds a significant commercial advantage for airliners.

Apart from commercial aircraft, the move to design modern combat aircraft with stealth capabilities has become a primary driver in the design process and has led to payload, which reflects radar, being stowed within bays. Before deployment, the bay is subjected to large pressure oscillations, capable of producing audible tones reaching levels up to 175 dB [5,6]. The tonal noise radiates into the far-field, compromising the stealth capability of the aircraft. The strong pressure oscillations can also lead to fatigue damage to the weapon's deployment mechanism.

Although noise reduction solutions exist in the form of liners, porous materials, and various aerodynamic devices, it is apparent that these passive solutions do not always work at off-design conditions and therefore have limited use in engineering applications. The demand for active acoustic control in aerodynamics has received less attention, because actuators are predominantly investigated to enhance aerodynamic performance. However, active

Presented as Paper 2802 at the 11th AIAA/CEAS Aeroacoustics Conference, Monterey, CA, 23–25 May 2005; received 19 July 2006; revision received 19 January 2007; accepted for publication 22 January 2007.

*Research Fellow, Aeronautics and Astronautics; scchan@soton.ac.uk.
†Professor, Aeronautics and Astronautics; x.zhang1@soton.ac.uk. Associate Fellow AIAA.
‡Professor, Aeronautics and Astroanutics; sbg2@soton.ac.uk.

devices such as piezoelectric actuators and blowing/suction jets are inherently fragile, posing installation and maintenance issues. Moreover, there are greater concerns with reliability and performance under extreme conditions such as icing or trapped debris. The aim is to develop a system that is reliable, relatively easy to install and maintain, and can adapt to a range of flow conditions.

An alternative actuation method is one that uses plasmas coupled with electric fields to manipulate the flow via particle collisions of the plasma to the neutral gas. The use of plasmas in flow control is not new; however, the recent invention that allows sufficient quantities of plasma to be produced efficiently [7] at atmospheric conditions means that flow control devices can be developed that yield an increase in performance at relatively low energy cost [8]. The principle of plasma flow control is to allow neutral species to be manipulated by an electric or magnetic field [8]. Through Lorentzian collisions, momentum is transferred to the neutral gas via charged particles in the plasma, thus affecting the flow around an aerodynamic surface. Several types of atmospheric pressure glow (APG) discharge plasma actuators were employed for flow control applications, two of which are the 1-atm uniform glow discharge plasma (OAUGDP) actuators and the dielectric barrier discharge (DBD) actuators. The difference between an OAUGDP and a DBD is the mechanism of plasma formation: the OAUGDP is characterized by a diffuse uniform glow and the DBD is characterized by filamentary microdischarges [9,10]. For inducing fluid motion using plasma actuators (OAUGDP and DBD), two common methods are used. The first type uses electric-field gradients of the electrodes, which produce the plasma, to move the fluid. This is known as paraelectric forcing, coined by Roth [8] for 1-atm OAUGDP actuators or steady actuation normally referred to for DBD actuators. The second method for inducing fluid motion is known as peristaltic forcing or phased actuation for OAUGDP and DBD actuator devices, respectively. This method uses a series of plasma actuators, whereby each actuator is activated consecutively through phase variations to drive the fluid along a surface. The application of 1-atm uniform glow discharge plasma actuators to flow control applications was initially performed by Roth et al. [11]. Using paraelectric-based actuators in a low-speed wind tunnel, Roth et al. discovered that symmetric electrode strips (Fig. 1a) aligned in the direction of the mean-flow-induced large vortices and increased drag. However, asymmetric electrode strips (Fig. 1b) aligned spanwise to the mean flow were able to increase the velocity of the fluid close to the surface.

The simplicity and absence of any mechanical moving parts (e.g., pumps) make it a desirable method for flow control applications. However, the technology can also be extended to aeroacoustic applications. The principle of using plasma actuators in aeroacoustics for noise control is to modify the flowfield to disrupt mechanisms of flow-induced noise. However, to develop a system that can be applied to engineering applications, the technology needs to be developed and optimized for the application. The work in this paper describes the attempt to use plasma actuators for the control of tonal noise, using a cavity as a test case.

The study of cavity flows has received a great deal of attention over the years from academia, industry, and, in particular, the automotive and aerospace sectors of industry. Examples of cavities in engineering include aircraft landing gear and weapons bays, sun roofs, car-door gaps, open windows in buildings, and high-lift devices on wings.

The research into cavity flows has been extensive and focus has varied, as evidenced by the different review papers devoted to the subject [12–15]. The simplest and most general form of cavity is the rectangular cavity. The cavity geometry is characterized by the length-to-depth ratio L/D for a two-dimensional (2-D) cavity and the length-to-width ratio L/W for a three-dimensional (3-D) cavity. The change in definition from length-to-depth to length-to-width for 2-D and 3-D cavities, respectively, signifies the dominant geometrical characteristics that govern the behavior of the flow. The type of flow regime experienced by the cavity is dependent on a number of parameters, including the geometry (L/D and L/W), Reynolds number, Mach number, oncoming boundary-layer displacement thickness, and momentum thickness [12].

The unsteady flowfield local to the cavity can cause rapid pressure fluctuations that lead to self-sustained oscillations. These self-sustaining oscillations were classified into three categories by Rockwell and Naudascher [12]: fluid dynamic, fluid resonant, and fluid elastic. Cavities with flow oscillations that are strongly coupled to a standing acoustic wave within the geometry are termed fluid resonant. The frequencies for this class of oscillation have wavelengths that are the same as, or lower than, the characteristic length or depth of the cavity. A cavity that exhibits fluid-elastic oscillations is the result of a periodic displacement or vibration of a solid boundary that is coupled with the oscillations. Fluid-dynamic oscillations describe the condition in which oscillations occur due to natural instabilities of the flow. The fluid moving over the cavity and the initial stagnant flow within the cavity create a shear. The shear leads to a Helmholtz instability, forming wave patterns [16], which is important for initiating the development of the roll up of the shear layer into discrete vortices that can be observed in cavity shear layers.

The instabilities of the shear layer that span a cavity [13] cause disturbances that convect downstream at a velocity κU_∞. The value of κ is approximately 0.6 for subsonic flows [17] and varies according to the cavity geometry, freestream flow, and boundary conditions [18]. The characteristics of the shear layer amplify these disturbances [19,20] and can either provide energy input to a transverse mode of oscillation or form part of a feedback mechanism for a longitudinal mode of oscillation [17]. The feedback mechanism was originally suggested by Rossiter [17], who investigated the flow over a range of rectangular cavities at subsonic and transonic speeds. The experimental work showed that cavities with $L/D > 4.0$ would be dominated by random pressure fluctuations, whereas for deeper cavities, the pressure fluctuations would be periodic. Rossiter proposed that vortices in the shear layer shed periodically from the leading edge of the cavity and convect downstream with the mean flow to the rear wall. The vortices interact with the wall, generating acoustic disturbances that travel back upstream within the cavity. On reaching the leading edge of the cavity, the acoustic waves disturb the shear layer, resulting in the shedding of new vortices, thus creating a feedback loop. As a result of the investigation, Rossiter derived a semi-empirical formula for predicting the tonal frequencies generated by the fluid-dynamic oscillations over a cavity, which was subsequently modified by Heller et al. [21] to account for supersonic flow conditions [Eq. (1)]:

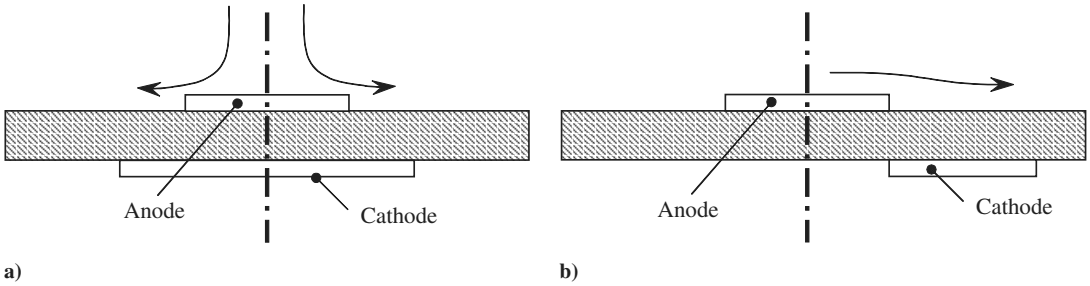

Fig. 1 Typical plasma actuator cross-sectional geometries with the direction of induced mean flow: a) symmetric and b) asymmetric about the anode centerline.

$$St = \frac{fL}{U_\infty} = \frac{a - \alpha}{1/\kappa + [M/\sqrt{(1 + [(\gamma - 1)M^2]/2)}]} \quad (1)$$

In the present study, plasma actuators were applied to the leading-edge boundary flow of a cavity. Flowfield and acoustic measurements were made of the cavity with and without plasma actuation. In the following sections, the experimental method and the results are presented.

II. Experimental Apparatus

A. Wind Tunnel

Experiments were conducted in a low-speed wind tunnel at the University of Southampton wind-tunnel facility. The wind tunnel [22] is of a closed-jet, open-loop design with a contraction ratio of 4:1 from the settling chamber to the main test section. Upstream of the settling chamber, a 12-blade axial fan is driven by a 4-kW, three-phase electric motor, providing a maximum fan speed of 1500 rpm. The maximum flow speed attainable in the working section of the tunnel is 25 m/s that is maintained to an accuracy of ± 0.04 m/s. The working section has a uniform cross section that measures 0.260×0.345 m and has a length of 0.850 m. The ceiling and port side of the tunnel test section are fitted with glass and Perspex panels that allow laser light to penetrate, and a camera to view, the test section from the outside for particle imaging velocimetry (PIV) measurements. To condition the flow, six screens of 18-gauge wire are located upstream of the test section, giving a freestream turbulence level of 0.3%. To acoustically treat the noise generated by the fan in the tunnel, a silencer chamber 0.5-m long was constructed and positioned between the fan and the wind-tunnel settling chamber. The walls of the silencer chamber were lined with 25-mm-thick open-cell acoustic foam to absorb noise radiated by the fan. In addition, the fan's line of sight to the wind-tunnel test section was also eliminated. The temperature of the air around the wind tunnel was closely monitored using a calibrated digital thermometer, but no temperature control was employed. The maximum temperature variation throughout a typical test run was ± 1.6 deg. The temperature variations were monitored to maintain the accuracy of the wind speed in the tunnel to ± 0.04 m/s.

B. Model Design

The model was designed as part of the floor of the wind tunnel, to minimize blockage [23,24]. This also allowed the model to be made larger, providing more scope for changing model configurations and running at a higher Reynolds number. The cavity model was designed to span the entire width of the test section, to minimize 3-D effects from the cavity side walls and to allow 2-D flow development across a greater proportion of the span of the cavity. The primary material used for the bulk construction of the model was 10-mm-thick transparent Perspex, held together with nylon screws. The stiffness of the Perspex ensured that any model vibrations were minimized. In addition, Perspex is a dielectric material and therefore would not interfere with the plasma actuators and their power source.

The model comprises three main sections: the leading-edge plate, the cavity section, and the trailing-edge plate. The model was designed to allow a cavity with a maximum dimension of 200×50 mm with $L/D = 4.0$. The geometry could be varied by replacing the trailing-edge wall with a solid-wood insert (Fig. 2). The model was designed so that the leading- and trailing-edge plates could be removed, allowing various plate lengths, which were constructed from the 1.6-mm-thick copper-clad board, to be fitted. A large number of possible test configurations were made possible by varying the distance between the insert and the leading-edge wall; however, the results presented are for a cavity with $L/D = 1.0$.

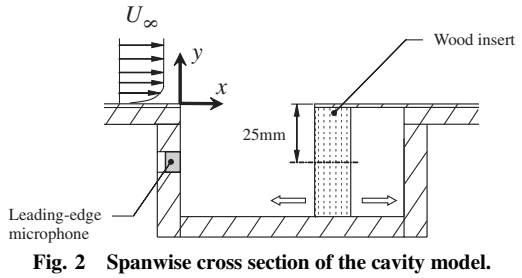

Fig. 2 Spanwise cross section of the cavity model.

C. Plasma Actuator Circuit and Fabrication

To generate an atmospheric glow discharge plasma, a sufficiently high potential is required to break down the surrounding species [25]. The potential is required at kilohertz frequency to sustain the glow discharge and prevent electron avalanches that lead to arcing. A signal from a frequency generator was used to operate a power metal-oxide-semiconductor field-effect transistor (MOSFET), which allowed a low dc voltage to pass through a step-up transformer at kilohertz frequency [7] and produce a high-voltage output.

A PICmicro microcontroller [26] was programmed to produce a periodic square-wave signal to switch the MOSFET at the desired frequency for the production of the plasma (Fig. 3). To program the microcontroller, the PICSTART Plus development kit (Microchip Technology Inc.) was used. The capability to program the PICmicro and control the individual output ports adds flexibility, to accommodate future actuator designs and control algorithms [27].

The purpose of the frequency generator was to modulate a dc input into a step-up transformer (Intermotor electronic ignition coil type 1134) that has a turn ratio of 1:150. The high-voltage output from the transformer is fed into a printed circuit board (PCB) that has electrodes of the plasma actuators etched into the copper surface of the PCB. PCBs are relatively inexpensive and simple to etch using a ferric chloride solution. The glass fiber/epoxy resin of the PCB has a dielectric constant of $K = 4.6$. For a 1.6-mm-thick PCB, the dielectric would be suitable for insulating the anodes from the cathodes up to 22.0 kV before electrical breakdown of the dielectric occurs.

The experimental work presented in this paper is based on steady actuation. The plasma actuators were a series of electrodes that were manufactured to be aligned with the mean flow. The cathodes were made wider than the anodes that were on the upper-flow-facing surface (Fig. 1a). The geometry of the electrodes was based on previous experimental work by Roth et al. [11], with the dimensions of the actuators chosen to introduce 3-D flow across the span of the cavity. For the etching process of the electrodes, a template was used to cover areas of copper that were required for the actuators. Once the template was applied, the entire board was immersed into a ferric chloride solution until the excess copper had dissolved. The board was taken out of the solution and cleaned before the template was removed. The high-voltage lead and ground wires were soldered to anode (Fig. 4a) and cathode (Fig. 4b) electrodes on the board.

D. Particle Imaging Velocimetry

The PIV system used in the experiments was produced by Dantec Measurement Systems and incorporates two Gemini Nd:YAG[§] lasers by New Wave Research that are capable of running at a 16-Hz double-pulse repetition rate, emitting 120 MJ pulses at 532-nm light frequency. A Dantec HiSense (type 13 gain 4) 1024×1289 resolution, charged coupled device (CCD) camera was used and operated in a double-frame mode to capture images of the flowfield at 2 Hz. The lenses available for the CCD camera were the Nikon-produced Nikkor 24, 60, and 105 mm type of $f2.8$ lenses. To provide seeding for the flow, a Safex S195G smoke seeder using Regular DJ Fluid (DJ mix) by Martin Professional was used. The typical sizes of the nonspherical particles were 2 μm in diameter. The particles provided suitable tracer material that was homogeneously distributed into the flow. The seeder was placed in the same room as the wind tunnel and care was taken so that the position of the seeder would not interfere with the flow around the wind tunnel.

The density of seeding particles produced by the Safex S195G smoke seeder is dependent on a number of factors, including ambient

[§]Yttrium aluminium garnet solid doped with neodymium.

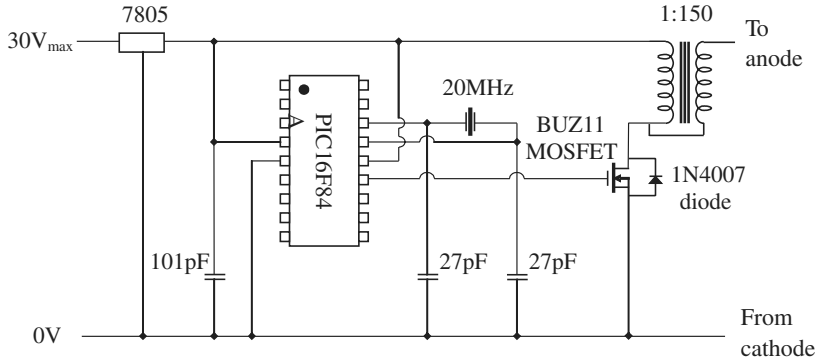

Fig. 3 Schematic of the microcontroller circuit to modulate the dc input to the transformer.

humidity and seeding-fluid properties. However, the smoke seeder is capable of providing a maximum seeding density of 1.50×10^{-4} kg/m^3. The atmospheric standard density of air at sea level is 1.22 kg/m^3. The density of the seeding particles is significantly small compared with the density of air (0.01%) and can be considered to have little effect on plasma formation.

For each experimental condition, 250 image sets of the flowfield were taken of the cavity geometry with and without plasma. PIV surveys in the $x - y$ plane were conducted on the model centerline at various flow speeds, ranging from $U_\infty = 10$ to 20 m/s. PIV surveys were also performed to acquire images from the $z - x$ and $z - y$ planes local to the plasma actuators at $U_\infty = 0$, 15, and 20 m/s.

Image correlations were performed using Dantec's FlowManager. Typically, each image set was processed using an adaptive correlation, with the smallest interrogation area available of 16×16 pixels and a 75×75% overlap adopted to improve the resolution of the vector map. The processing technique produces a vector map containing up to 317×253 vectors, typically representing every square millimeter of the flowfield with a vector. Inevitably, spurious vectors arise as a result of the finite number of tracer particles in the flow, excessive particle displacements, insufficient resolution, or even poor image quality [28]. The method for removing these spurious vectors, or outliers, is by using a range validation whereby vectors that are greater than a specified magnitude would be rejected.

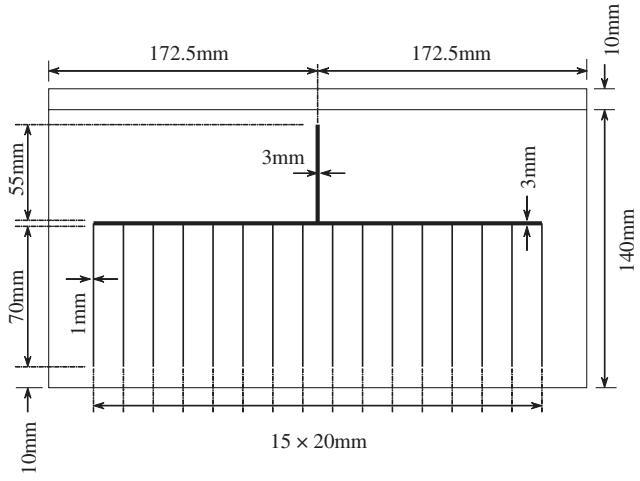

a)

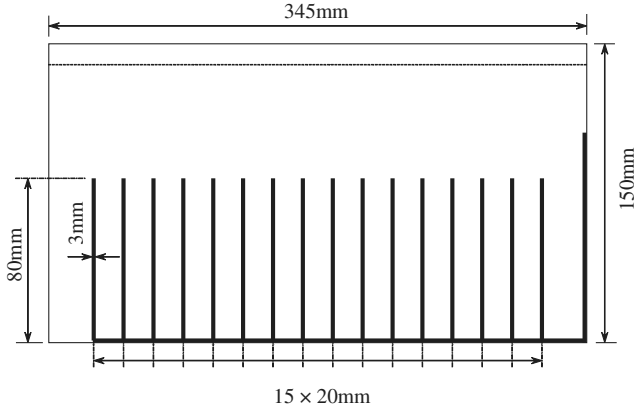

b)

Fig. 4 Layout of the symmetric electrodes manufactured using PCBs: a) anodes and b) cathodes.

E. Pressure Measurements

Surface pressures of the cavity were recorded using a Panasonic WM-60A omnidirectional condenser microphone. The microphone was used to measure the pressures on the front wall of the cavity, which was connected to a sound card in a PC via a preamp. The sampling frequency for all microphone measurements was 44,100 Hz, to capture the audible-frequency spectra.

To process the signals, a Matlab script was developed to convert the raw data into Fourier space. A 4096-point fast Fourier transform (FFT) with zero overlap was applied to each signal block. To reduce spectral leakage, a Hanning window function was applied to each signal block before performing the FFT. The frequency plots were averaged over 300 signal blocks, for statistical confidence in the results.

III. Experimental Setup

Before installing the cavity model into the wind tunnel, it was necessary to determine the existence of a pressure gradient on the floor of the test section. To determine the existence of any pressure gradients, a series of surface-pressure measurements were recorded at discrete locations from the centerline of the wind-tunnel test section. Measurements showed that the maximum variation in the pressure coefficient along the entire length of the test section was $\Delta C_p = -0.05$. The favorable pressure change corresponds to a velocity increase of 0.1 m/s for $U_\infty = 25$ m/s, which is a variation of less than 0.5%. The observed gradient is the result of boundary-layer growth on the walls of the wind-tunnel test section. The artificial constriction imposed by the boundary layers increases the local fluid velocity that results in a favorable pressure gradient.

A. Model Installation

To provide the appropriate boundary conditions, a fixed-length leading-edge plate was used. During the study, various boundary-layer conditions were explored in an attempt to generate cavity tones. Results showed that using a 150-mm-long plate with a sharp leading edge produced the appropriate boundary conditions and strong cavity tones. The theoretical laminar boundary-layer thickness at the upstream edge of the cavity was 5.9 and 4.9 mm for $U_\infty = 10$ and 20 m/s, respectively, satisfying the nondimensional length parameter of Sarohia [29]. It should be noted that applying a trip strip to the leading edge of the model resulted in no tones being observed and the frequency spectra were broadband.

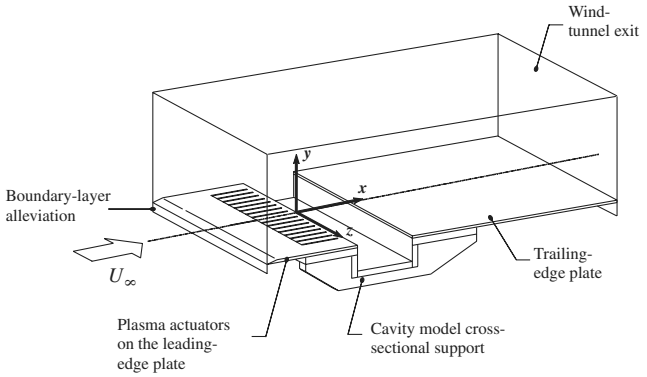

Fig. 5 Schematic of the cavity model showing the PIV setup configuration to capture images in the $x - y$ plane.

Because of the buildup of a boundary layer within the wind-tunnel contraction and to prevent the wind tunnel's boundary layer upstream of the test section from interfering with the flat-plate boundary layer of the model, it was necessary to bleed some of the air out before the test section. Based on velocity profiles from a PIV survey over the floor of the empty wind tunnel, the entire model was raised 10 mm so that the boundary layer could bleed underneath the model into the ambient air (Fig. 5). Once an oscillating cavity flow was established, baseline flowfield surveys for the cavity were performed for comparison with the plasma actuator case.

B. Measurement Systems Setup

The PIV measurement system was set up so that the shear-layer and recirculation regions within the cavity could be captured. The CCD camera was located outside the wind-tunnel working section. To capture images of the flow in the $x - y$ plane, the camera was pointed in the direction along the width of the cavity (Fig. 5). The laser system that provides the illuminating light sheet was mounted on a Dexion support above the glass-panel ceiling of the wind tunnel. The light sheet was aligned to the centerline of the model that was perpendicular to the lens of the CCD camera. Efforts were also made to capture images of the flowfield around the plasma actuators in the $z - y$ and $z - x$ planes. To minimize any reflections of the laser sheet from the Perspex surfaces, satin black paint was sprayed over the surfaces of the model to improve the quality of the data near the walls.

The microphones employed for unsteady pressure measurements were flush-mounted to the leading-edge wall of the cavity model along the centerline (see Fig. 2). Before installation, the microphones were calibrated with a Brüel & Kjær pistonphone (type 4230). The pistonphone produced a steady output signal of 1 kHz at 88.1 dB, which was recorded by the microphone. The FFT was applied to the recorded signals, and the dominant tone for each signal was adjusted to match the values produced by the pistonphone. The adjustments to the frequency and sound pressure level during the calibration process were used in the processing of measured pressure data during the tests.

C. Error and Uncertainty

Acoustic measurements were conducted throughout the period of the research; however, the errors for a specific microphone are not easily quantifiable. The main causes of uncertainty are the variation of temperature and the variation of the freestream flow during data acquisition. To help minimize temperature variations, the wind tunnel was run for a short period of time, typically for 30 min, to allow the temperature of the microphone and the air around the facility to stabilize. For periods of data acquisition, the wind tunnel was maintained to an accuracy of ± 0.040 m/s. In addition, the microphones were calibrated at the start and the end of a test day with a Brüel & Kjær pistonphone (type 4230). An FFT was applied to the recorded calibration signal to produce a frequency spectrum. The tone in the spectrum was adjusted to match the values produced by the pistonphone. The amplitude and frequency of a signal in the spectrum is dependent on the sampling rate of the original signal, the resolution of the FFT, and the number of blocks the signal is averaged over. For the acquisition of data, the sampling rate of 44,100 Hz was used and the signals were processed using a 4096 FFT; however, for statistical confidence in the result, the FFT signal was averaged over a number of blocks.

The errors within typical PIV measurements were calculated based on the mathematical derivation by Maina [22]. The positional error of the vectors on a PIV vector map is related to the resolution of the CCD camera. The CCD resolution is determined by the hardware and is fixed. The values for the scale factor and the time between laser pulses are determined by the experimental setup and flow conditions. The uncertainty in the position of the vectors was estimated to be 0.1 mm in the horizontal and vertical axes. However, this value is small compared with the uncertainty in the cavity geometry that was manufactured to an accuracy of 0.5 mm. The uncertainty in the velocity for an instantaneous vector was estimated to be 0.12 m/s. However, a typical data set comprises 250 image pairs and, therefore, the uncertainty in a time-averaged vector is 7.6×10^{-3} m/s.

The error and uncertainties in boundary-layer measurements were estimated for measured properties using the single sample uncertainty analysis described by Moffat [30]. The measurement accuracy of the micrometer was ± 0.013 mm, and the digital manometer read to an accuracy of $\pm 0.50\%$ of the freestream value. The typical temperature variation throughout a test was ± 1.6 deg, and the wind tunnel was maintained to an accuracy of ± 0.040 m/s. The skew angle of the Preston tube was estimated to be ± 2.0 deg. The uncertainty in reading the u velocity component was estimated to be 0.152 m/s at a freestream speed of 20 m/s. However, the stated values represent the worst case; the smoothness of the data suggests that the uncertainty is much lower.

IV. Results and Analysis

A. Aerodynamic Flowfield

Oil-flow visualization was performed to provide a visual analysis of the streamwise and spanwise development of the flow over the surface of the model. A solution of ultraviolet powder pigment and paraffin was tenuously applied to the entire surface of the model and care was taken to minimize streaks that would impair the visualization. After applying the solution, the wind tunnel was set to a constant flow speed to allow the solution to assume the characteristics of the surface flow as it dried.

Surface streak lines showed that the spanwise flow within the cavity was largely 2-D. The surface flow results for the cavity with $L/D = 1.0$ (Fig. 6) show that the spanwise line of separation is near parallel with the front and rear walls of the cavity, in which the flow is nominally 2-D. The 2-D region of the flow spans approximately 88% of the cavity width. At the end-wall regions, 3-D effects are observed. The surface streak lines reveal a large portion of 2-D flow; it follows that the mean flow across the cavity is also largely 2-D.

PIV surveys in the $x - y$ plane were conducted on the model centerline for a cavity with $L/D = 1.0$ at flow speeds ranging from $U_\infty = 10$ to 20 m/s. For each experimental condition, 250 image sets of the flowfield were acquired. Particle imaging velocimetry

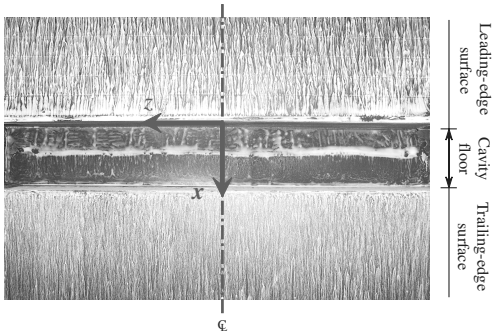

Fig. 6 Surface streak lines on the cavity floor for $L/D = 1.0$ at $U_\infty = 20$ m/s; flow is from top to bottom.

surveys in the $x - y$ plane show the development of the shear-layer and recirculation regions within the cavity. The temporal resolution of the CCD camera was 2 Hz, which is significantly lower than the frequency of the cavity oscillations, hence only instantaneous snapshots of the flow and not a time-resolved series of the flow could be attained. Instantaneous contours of spanwise vorticity $\Omega_z = (\partial v/\partial x) - (\partial u/\partial y)$ show discrete vortices that convect downstream in the shear layer for the cavity (Fig. 7). The convection of the vortices in the shear layer directly from the leading edge to the trailing edge shows that the cavity flowfield is of an open-flow regime [31]. The geometry and oncoming boundary conditions largely dictate the flow regime and mode of oscillation that occurs in the cavity [31]. The contour plots in Fig. 7 also show vorticity upstream of the cavity. The negative vorticity is a result of the no-slip condition at the wall, which produces a velocity gradient $\partial u/\partial y$. The hump shown in the approaching boundary layer is the result of reflections creating spurious vectors during the correlation process affecting the data in the region near the wall.

A plot of frequency spectra using the pressure signal from the front wall of the cavity shows a dominant tone of oscillation that scales with freestream velocity for the cavity with $L/D = 1.0$ (Figs. 8a and 8b). The dominant peaks of the spectra represented in Fig. 8a occur at a different value of Strouhal number based on cavity length to the dominant peaks of the spectra, shown in Fig. 8b. The theoretical values for the Strouhal number were calculated using Eq. (1), in which $\alpha = 0.0$, $\gamma = 1.4$, and $\kappa = 0.6$, and the freestream speed of sound is 340.5 m/s. The jump in the Strouhal number indicates a change in the Rossiter mode;

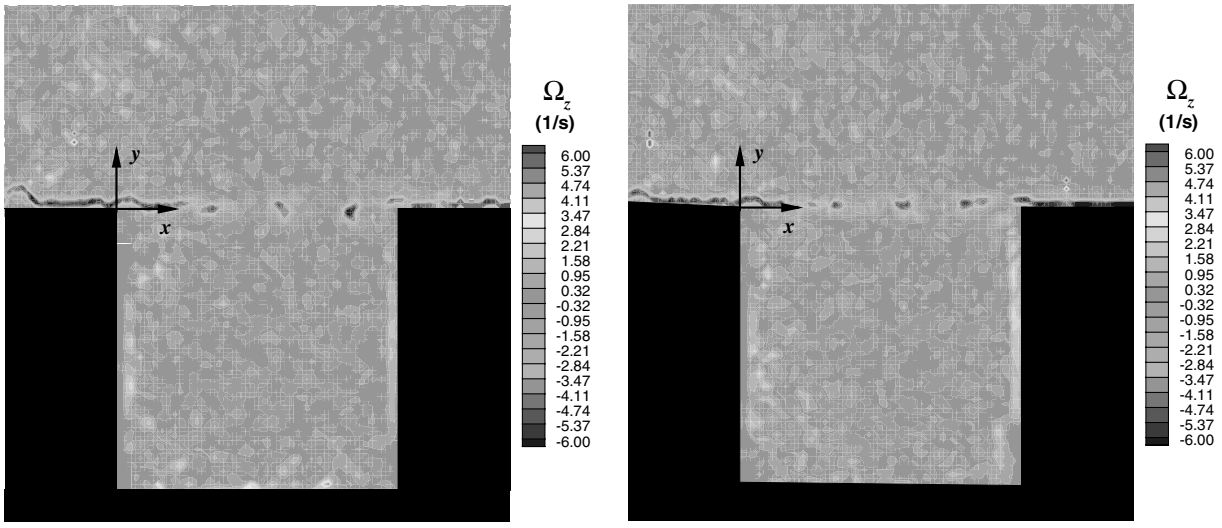

Fig. 7 Instantaneous samples of processed PIV images displaying contours of vorticity Ω_z; $L/D = 1.0$ and $U_\infty = 10$ m/s.

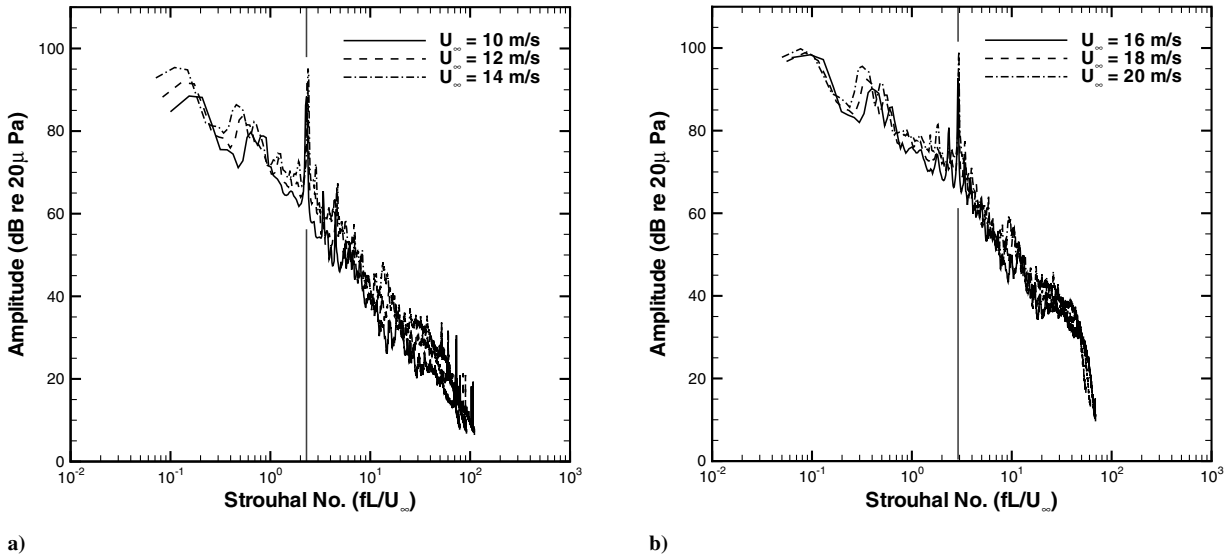

Fig. 8 Amplitude spectra for a cavity with $L/D = 1.0$; the calculated Rossiter mode is indicated by the vertical line.

Table 1 Dominant tones for a cavity with $L/D = 1.0$ at $U_\infty = 10$ to 20 m/s

U_∞, m/s	f, Hz	St_{exp}	St_{theory}	Mode
10	442	2.210	2.358	4
12	549	2.287	2.350	4
14	661	2.361	2.342	4
16	915	2.859	2.918	5
18	1055	2.931	2.908	5
20	1173	2.933	2.898	5

however, for a given Rossiter mode, the dominant peak frequency is shown to scale with velocity (Table 1).

The solid ceiling of the wind-tunnel test section is 0.260 m above the mouth of the cavity, which can reflect noise and cause an excitation of the duct modes in the test section [32]. The frequencies of oscillation for these duct modes is defined by Eq. (2). For the values of $n = 1$ and 2, the corresponding duct mode frequencies are 549 and 1098 Hz. However, the peaks in the spectra displayed in Fig. 8 scale well with velocity, indicating a relationship between the Strouhal numbers and hydrodynamic instabilities of the flow.

$$f_{duct} = \frac{c(n+1)}{2(h+D)} \tag{2}$$

B. Plasma-Actuator-Induced Flowfield

To determine the performance characteristics of the plasma actuator array and to provide insight into the development of the time-mean-induced flowfield, the operating voltage of the plasma actuators was varied. The output voltage from the transformer was controlled by the input supply voltage. For the investigation, the input voltage was varied from 10 to 30V_{dc} in 5-V increments. The dc voltage was effectively oscillated at 3.2 kHz across the transformer to generate output voltages in the kilovolt range at the desired frequency (Table 2). To accurately determine the input power to the transformer, a digital multimeter was used to measure the voltage and current, from which the power consumption was determined. The high-voltage output from the transformer was measured using a Testec high-voltage probe (TT-HVP 15HF) connected to a Goldstar oscilloscope (type OS-9020A).

A PIV survey of the flowfield around the plasma actuators was conducted under a no-flow condition in the wind tunnel. Instantaneous vector maps show a pair of counter-rotating vortical structures in the $z - y$ plane formed between adjacent actuators

Table 2 Supply voltage to the transformer and the corresponding output to the plasma actuators

Input voltage, V_{dc}	ν_0, kHz	Output voltage, kV_{pp}	IV_{dc}, W
10	3.2	5.8	2.0
15	3.2	8.8	10.5
20	3.2	11.6	22.0
25	3.2	14.0	37.5
30	3.2	16.0	55.5

(Fig. 9). These structures were reported previously in observations made by Roth et al. [33] through smoke-wire visualization on similar actuator geometry. The symmetric geometry of a single plasma actuator produces a localized spanwise velocity w on the surface. Although the plasma generated by a single actuator does not directly influence the fluid beyond the region of the plasma, the local plasma–fluid interaction creates a downwash directly above the actuator surface. The alignment of plasma actuators in a side-by-side configuration induces a spanwise motion of the fluid in opposing directions on the surface. This promotes a local region of upwash between the adjacent actuators. The localized regions of upwash and downwash create large counter-rotating vortex pairs in the streamwise direction $[\Omega_x = (\partial v/\partial z) - (\partial w/\partial y)]$ between the adjacent electrodes (see Fig. 10) and smaller vortices closer to the surface.

The time-mean-induced flowfield by the plasma actuators is shown in Fig. 9. The results in the figure are for the plane $x/D = -0.2$. For comparison, the figure shows the induced flowfield by the plasma actuators operating at 8.8 and 16.0 kV_{pp}. In the figure, the black regions represent the solid surface of the PCB dielectric and the light gray areas represent the location of the anodes and their surrounding plasma.

The induced flowfield around a plasma actuator, shown by the vector maps in Fig. 9, produces fluid motion along the surface of the dielectric and a region of downwash directly above the actuator. The neutral fluid is driven along the surface of the dielectric in a mean direction corresponding to the z axis away from an electrode. The presence of an adjacent plasma actuator creates upwash of the fluid, which is eventually entrained back into the downwash of the adjacent actuators. As a result, organized counter-rotating vortical structures are formed between a pair of plasma actuators (Fig. 10). Despite the plasma actuators being uniform and identical, the shape and size of the vortical structures vary between actuator pairs. However, the organized flow structures and the downwash above the plasma actuator show that fluid motion is achieved through electrostatic forcing and not thermal convection.

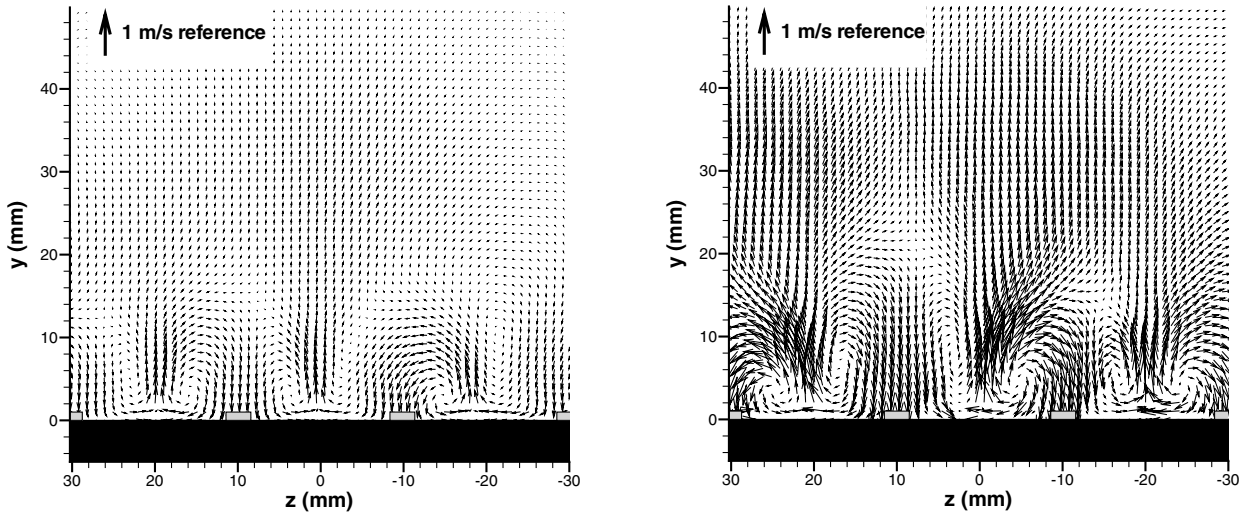

a) b)

Fig. 9 Cross-plane time-mean velocity-vector field at $x/D = -0.2$; plasma actuators operating at a) 8.8 kV_{pp} and b) 16.0 kV_{pp}.

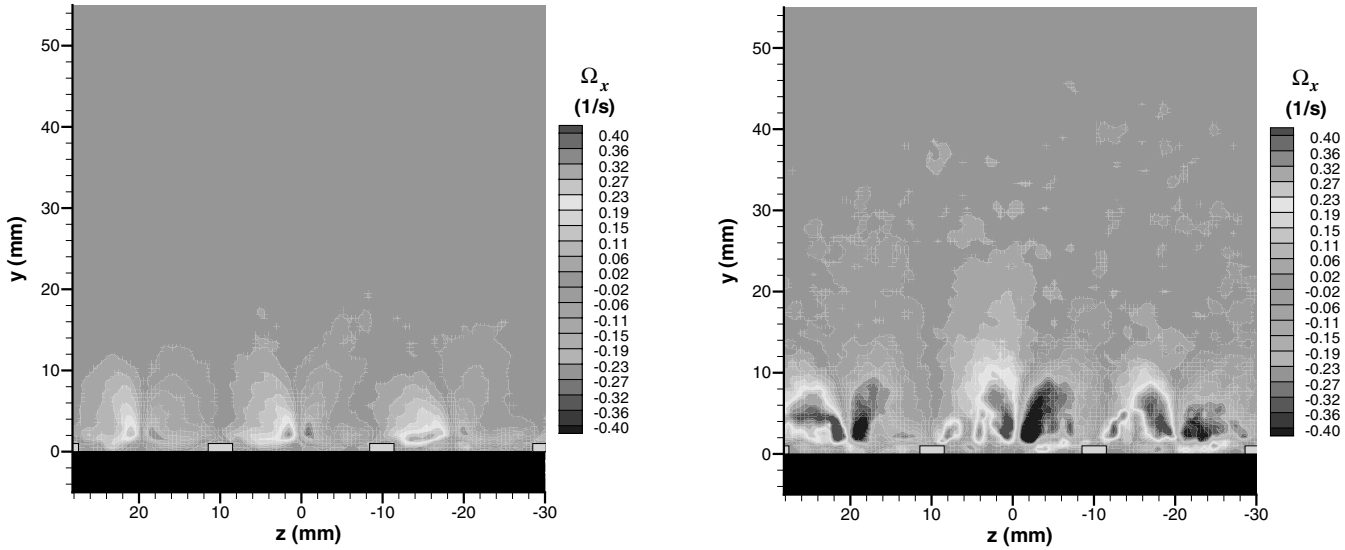

Fig. 10 Contours of the time-mean vorticity in the cross plane at $x/D = -0.2$; plasma actuators operating at a) 8.8 kV_{pp} and b) 16.0 kV_{pp}.

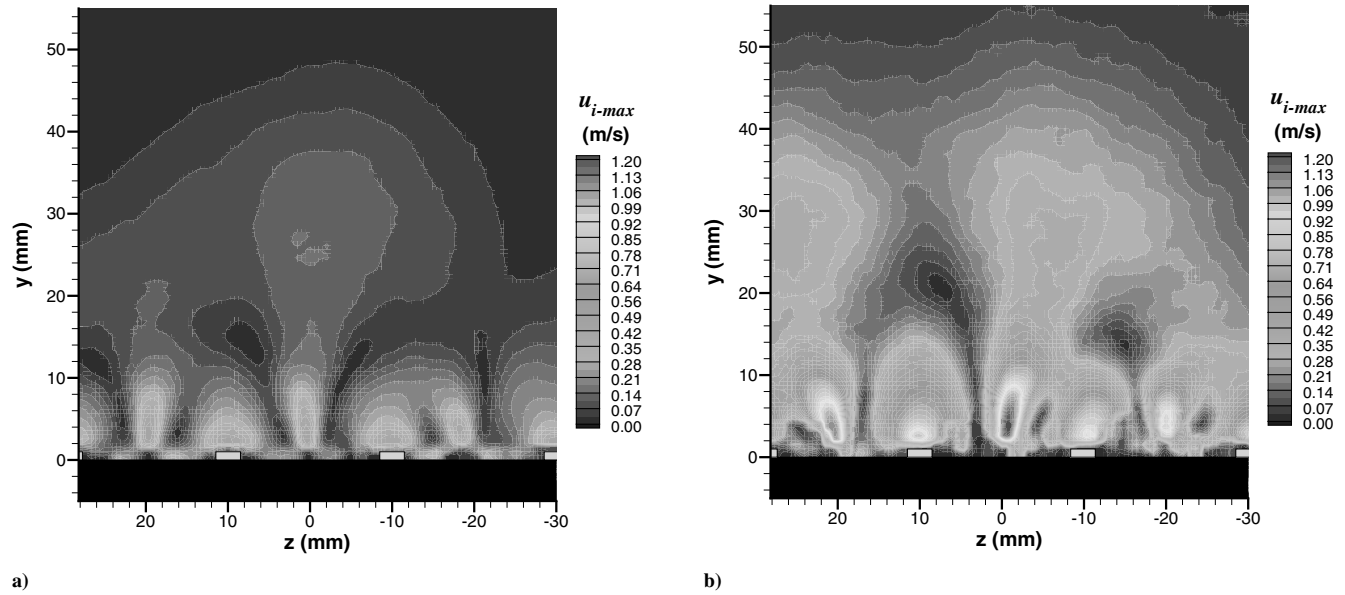

Fig. 11 Contours of the time-mean-induced velocity in the cross plane at $x/D = -0.2$; plasma actuators operating at a) 8.8 kV_{pp} and b) 16.0 kV_{pp}.

The time-mean flowfield for the plasma actuators operating at 16.0 kV_{pp} is shown in Figs. 9b and 10b. The time-mean-induced flowfield by the plasma actuators operating at 8.8 kV_{pp} is shown in Figs. 9a and 10a. For the plasma actuators operating at 16.0 kV_{pp}, the mean distance between the centers of two counter-rotating vortical structures in the z and y directions is $\langle d_z \rangle = 7.63$ mm and $\langle d_y \rangle = 2.32$ mm. For the plasma actuators operating at 8.8 kV_{pp}, the mean distance between the centers of two counter-rotating structures is $\langle d_z \rangle = 7.23$ mm and $\langle d_y \rangle = 4.93$ mm.

The magnitude of the time-mean-induced velocities operating at 8.8 and 16.0 kV_{pp} are shown in Fig. 11. For the cases studied, the maximum velocity was observed in the upwash between actuators. The maximum induced velocities are $\langle u_{i\text{-max}} \rangle = 0.61$ m/s and $\langle u_{i\text{-max}} \rangle = 1.28$ m/s for the actuators operating at 8.8 and 16.0 kV_{pp}, respectively.

An analysis of the mean velocities revealed that the maximum induced velocity did not scale according to $V_{pp}^{7/2}$, as determined by Enole et al. [34]. However, the relation was derived from experimental data using an asymmetric electrode arrangement in which the fluid was driven in one direction. The electrodes in this investigation are aligned in parallel next to each other, and the induced fluid motion by one plasma actuator opposes the induced fluid motion (in the z direction) by adjacent actuators. The data from the PIV surveys suggest that the induced velocity for this actuator arrangement is proportional to $V_{pp}^{5/4}$ supplied to the actuators (Fig. 12).

V. Cavity and Plasma Flowfield

The use of symmetric plasma actuators aligned in the streamwise direction to the oncoming flow to the cavity can lead to an attenuation of the dominant cavity tone. The induced flow from the plasma actuators generates spanwise variations in the boundary layer that can alter the development of the shear layer and thus the development of the discrete spanwise vortices that are important to cavity-mode oscillations.

A. Acoustic Measurements

The importance of the oncoming boundary conditions and the development of the shear layer for cavity-flow-induced noise are important for the tonal noise radiated by the cavity. To influence the fundamental mechanism of the flow-induced tonal noise, stream-

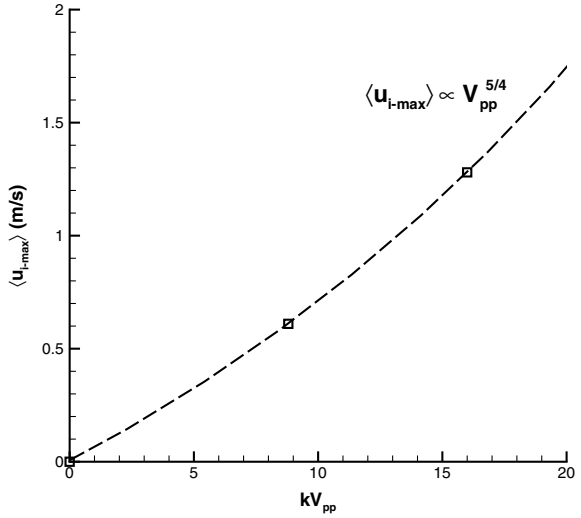

Fig. 12 Mean-induced velocity against input voltage to the plasma actuators.

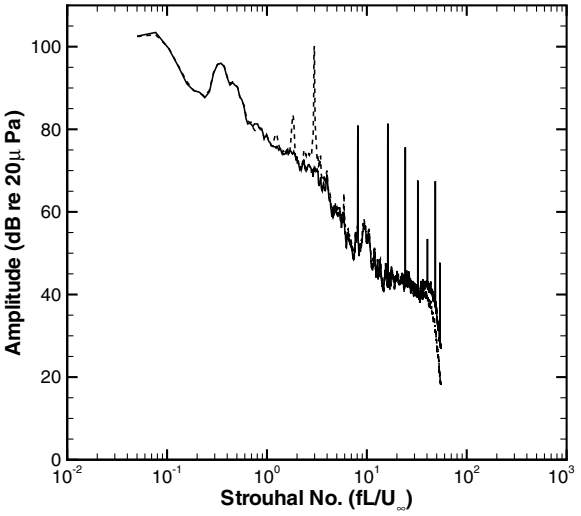

Fig. 13 Amplitude spectra for a cavity with $L/D = 1.0$ and $U_\infty = 20$ m/s; actuators active (solid line, 16.0 kV$_{pp}$) and actuators inactive (dashed line).

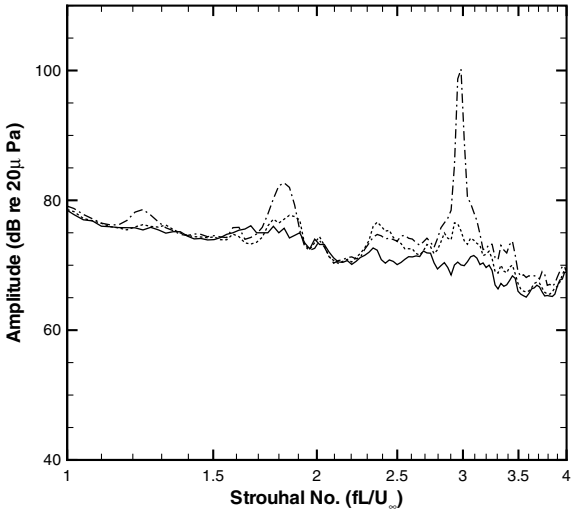

Fig. 14 Amplitude spectra for a cavity with $L/D = 1.0$ at $U_\infty = 20$ m/s; plasma actuators operating at 5.8 kV$_{pp}$ (dotted-dashed line), 11.6 kV$_{pp}$ (dashed line), and 16.0 kV$_{pp}$ (solid line).

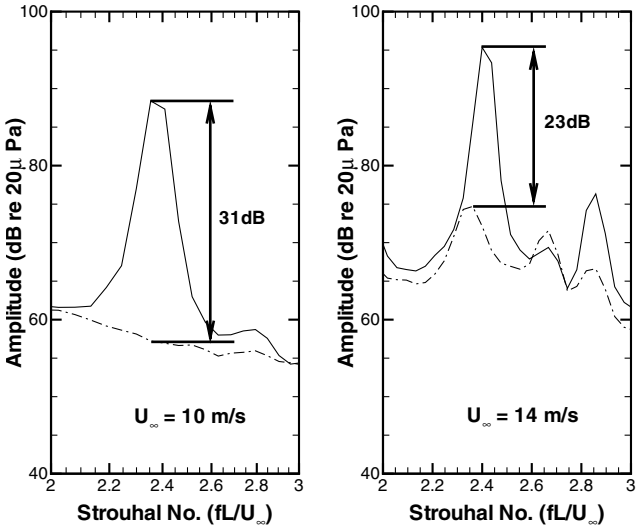

Fig. 15 Amplitude spectra for a cavity with $L/D = 1.0$ at $U_\infty = 10$ and 14 m/s; actuators inactive (solid line) and actuators active (dotted-dashed line, 10.8 kV$_{pp}$).

wise-aligned plasma actuators were located on the upstream surface approaching the cavity (Fig. 5), to influence the boundary layer and the development of the shear layer [18,35]. The plasma actuators were designed to create disturbances upstream of the cavity, to impede the development of the discrete vortices shed from the leading-edge corner of the cavity.

The flow-induced tonal noise observed in the frequency spectra was attenuated when the plasma actuators were activated (Fig. 13). The figure shows that the dominant flow-induced tone and its harmonics are attenuated to a level that is not discernible from the broadband noise level. The spectra shown in the figure are for the cavity at $U_\infty = 20$ m/s, but are representative of the results for the lower freestream-flow velocities investigated, with the plasma actuators operating at 16.0 kV$_{pp}$. During the measurements, it was observed that the effect of the plasma actuators was instantaneous, because flow-induced tones were attenuated immediately after the plasma actuators were activated.

In terms of attenuating the amplitude of the flow-induced tones, the performance of the actuators increased as the operating voltage was raised (Fig. 14). It was observed that for the plasma actuators operating at a constant voltage, an increase in the freestream velocity did not affect the actuator's ability to generate plasma. However, it was observed that higher operating voltages were required by the plasma actuators to attenuate the amplitude of the flow-induced tones to broadband level. This suggests that the loss in performance is the result of the induced flow by the plasma actuators having reduced effect on the cavity flow and acoustic fields as freestream velocity is increased (Fig. 15).

For the conditions in which the plasma actuators were activated, discrete tones in the higher-frequency range in the frequency spectrum can be observed. The frequencies of the tones correspond to the operating frequency of the plasma actuators (3.2 kHz) and its harmonics. The tones radiated from the plasma actuators are the result of wave propagation due to the formation and collapse of the induced electric field [36] around the electrodes. The formation and collapse of the electric field is a result of the high voltage supplied to the electrodes at 3.2 khz. The amplitude of the tones produced by the plasma actuator array increased with their operating voltage; their initial rate of increase, however, reduced as the input power was increased (Fig. 16). Higher values of input were limited by the maximum voltage output by the power supply unit.

A comparison of the overall sound pressure level was determined by integrating the spectra for the cavity $L/D = 1.0$ at $U_\infty = 20$ m/s, with and without plasma actuation. It was revealed that a reduction in the overall sound pressure level of 22% was achieved with the

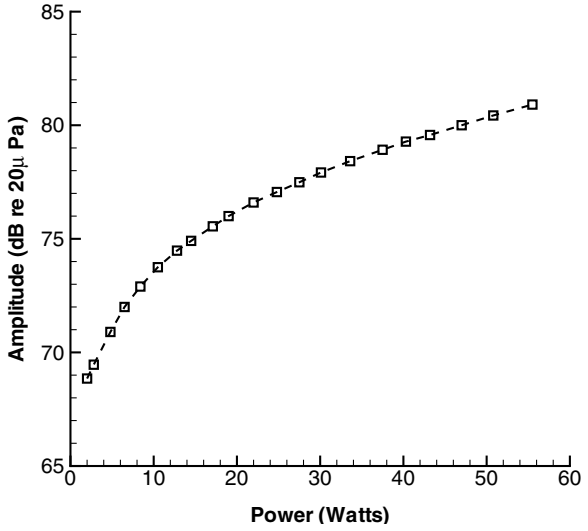

Fig. 16 Amplitude of the radiated tone at 3.2 kHz from the plasma actuator against input power.

plasma actuators activated for this case. Despite the plasma actuators producing high-frequency narrowband peaks in the spectrum, they represent a lower proportion of the overall sound pressure level compared with the cavity tone.

B. Boundary-Layer Survey

To characterize the flow conditions upstream of the cavity when the plasma actuators were activated, boundary-layer surveys were performed. Measurements were conducted using a Preston tube on the model centerline. To determine the 3-D effects of the induced flow on the boundary-layer profile, measurements were conducted at two separate spanwise locations: $z/D = 0.0$ and 0.2. The spanwise locations correspond to a point directly in line with an actuator and a point halfway between a pair of actuators. The boundary-layer profiles were measured at $x/D = -0.1$ for the plasma actuators operating at 8.8 and 16.0 kV_{pp}.

The boundary-layer profiles for the cavity with $L/D = 1.0$ are shown in Fig. 17. The results shown are for the freestream velocity $U_\infty = 20$ m/s, but are representative of the results at the lower freestream values investigated. Figure 17a corresponds to the boundary-layer profiles measured from the center between two actuators. Figure 17b corresponds to the boundary-layer profiles measured in line, downstream of an actuator. The figure shows that the plasma actuators can have a substantial influence on the boundary-layer profiles.

Table 3 Boundary-layer properties

z/D	V_{pp}, kV	U_∞, m/s	δ, mm	δ^*, mm	θ, mm	H
0.0	0.0	10	2.41	5.99×10^{-1}	3.03×10^{-1}	1.98
	8.8	10	2.54	7.16×10^{-1}	3.38×10^{-1}	2.12
	16.0	10	4.44	7.16×10^{-1}	3.02×10^{-1}	2.37
	0.0	20	1.77	3.08×10^{-1}	1.79×10^{-1}	1.72
	8.8	20	1.77	3.28×10^{-1}	1.90×10^{-1}	1.73
	16.0	20	2.16	5.54×10^{-1}	2.67×10^{-1}	2.08
0.2	0.0	10	2.41	6.11×10^{-1}	2.94×10^{-1}	2.08
	8.8	10	1.01	1.19×10^{-1}	8.60×10^{-2}	1.39
	16.0	10	0.50	2.60×10^{-2}	2.33×10^{-2}	1.11
	0.0	20	1.90	3.44×10^{-1}	1.99×10^{-1}	1.73
	8.8	20	1.52	1.30×10^{-1}	9.66×10^{-2}	1.34
	16.0	20	0.50	2.71×10^{-2}	2.20×10^{-2}	1.23

As the operating voltage of the plasma actuators is increased, the boundary-layer profiles at $z/D = 0.2$ become thinner and develop fuller profiles (Fig. 17b). The increase in the velocity near the surface of the actuators is most likely to be the result of the induced downwash from the plasma actuators (Fig. 9) entraining the high-speed flow. Similar boundary-layer profiles observed at $U_\infty = 10$ m/s would appear to support this observation, rather than the actuators directly producing the high velocities. The boundary-layer profiles at $z/D = 0.0$ exhibit the opposite behavior to the profiles measured at $z/D = 0.2$. In this case, the boundary layer is influenced by the upwash induced by the plasma actuators, leading to a thickening of the boundary layer, with a shallower profile as the operating voltage of the plasma actuators is increased (Fig. 17a).

Details of the measured boundary-layer properties are summarized in Table 3. In the table, the data show that the plasma actuators have a reduced effect on the flow as the freestream velocity is increased when the operating voltage is constant.

Despite the spanwise variation in the boundary-layer profiles (Table 3), the thickness of the boundary layer is sufficient for shed vortices to develop from the cavity leading edge [29].

C. Streamwise-Flow Development

For the various flow conditions investigated, the flow over the cavity was found to be highly unsteady and dominated by the characteristics of the shear layer (Fig. 18). The results shown are for $U_\infty = 20$ m/s in the plane $z/D = 0.0$, but are representative of the data obtained at the lower speeds investigated. The shear layer was characterized by discrete vortices that originate from the leading-

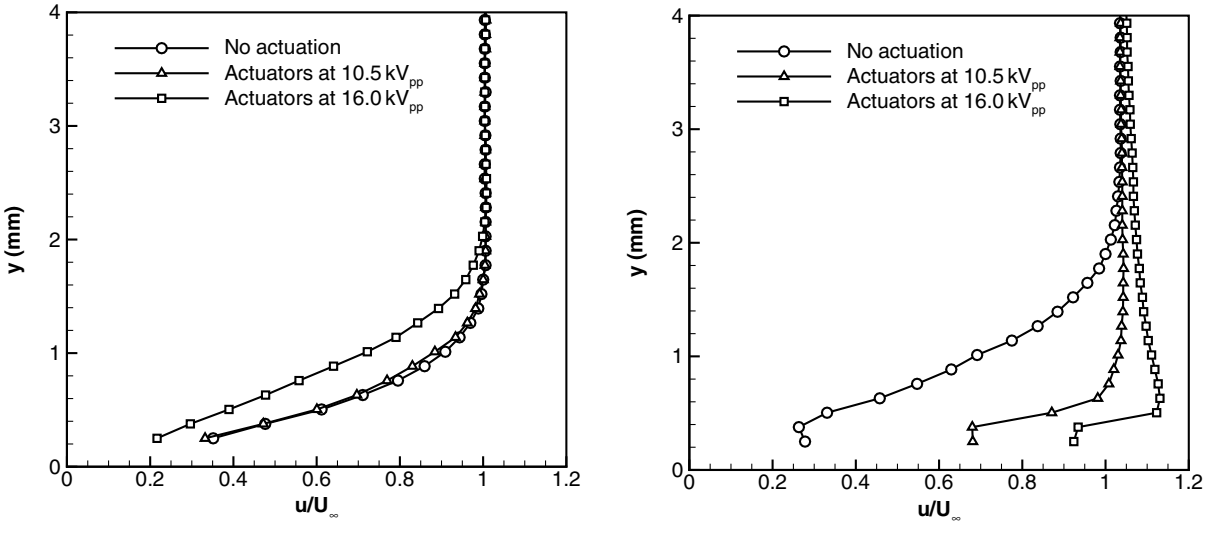

Fig. 17 Boundary-layer survey at $x/D = -0.1$ for $U_\infty = 20$ m/s: a) $z/D = 0.0$ and b) $z/D = 0.2$.

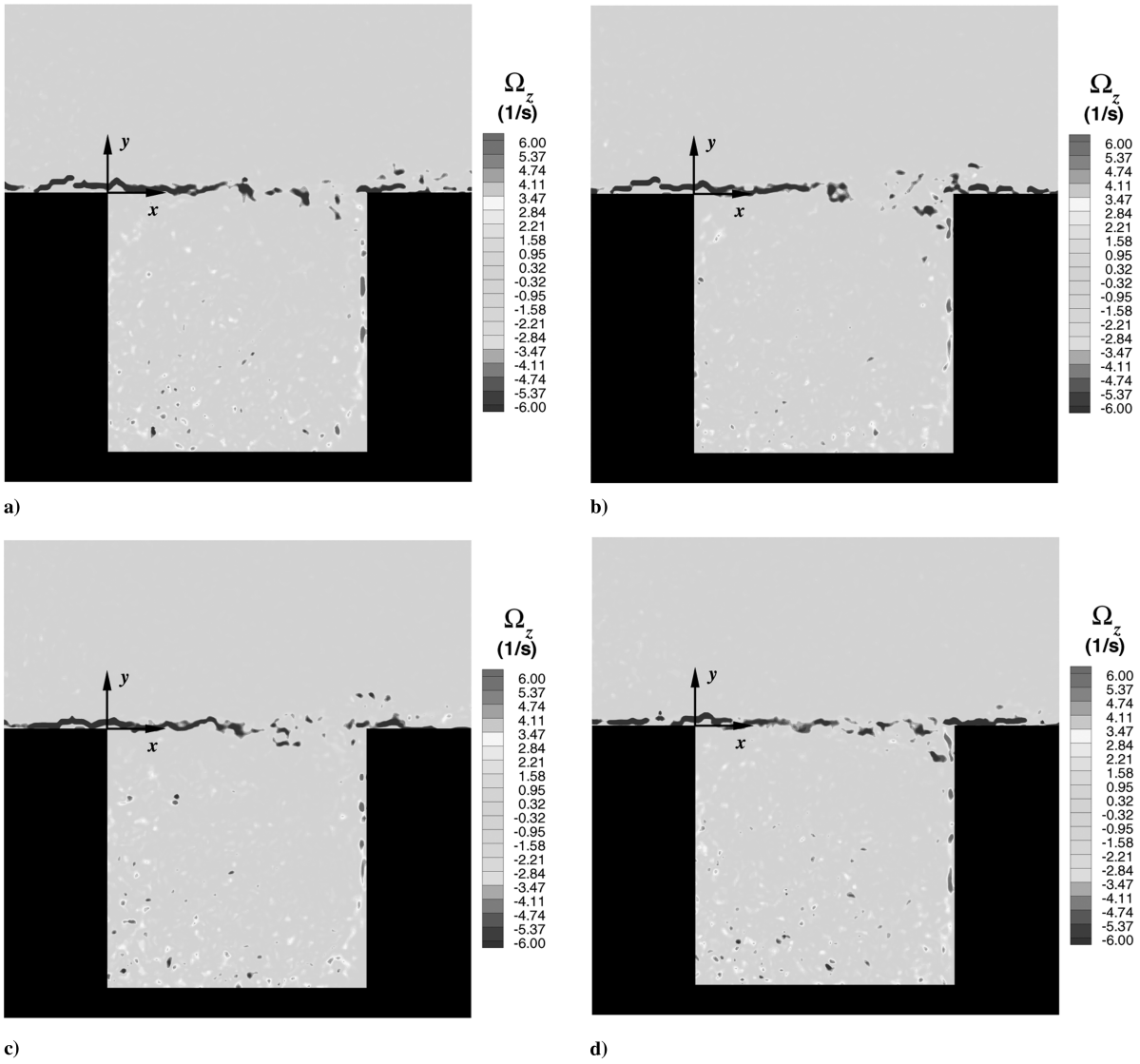

Fig. 18 Instantaneous samples of processed PIV images displaying contours of vorticity Ω_z for a cavity with $L/D = 1.0$ and $z/D = 0.0$ at $U_\infty = 20$ m/s; plasma actuators operating at 16.0 $\mathrm{kV_{pp}}$.

edge corner of the cavity and impinge on the trailing edge. It was observed that a large number of processed images, similar to those in Figs. 18c and 18d, were devoid of organized discrete vortices in the cavity shear layer. The intermittent nature of discrete vortices impinging on the trailing-edge corner of the cavity affect the feedback mechanism that is important for self-sustained cavity oscillations.

To determine if small-scale fluctuations were masking the discrete vortices in Fig. 18, a Galilean analysis [37] was performed on the instantaneous vector maps. For the analysis, the convective velocity of the vortices in the shear layer was taken to be $U_\infty = 0.6$ [17]. The analysis revealed a number of images displaying clear vortical structures in the shear-layer region, originating from the cavity leading edge (Fig. 19a). On the other hand, it was also observed that a large number of vector images processed using Galilean analysis lacked discrete vortical structures in the shear layer (Fig. 19b), confirming the intermittent nature of discrete vortices in the cavity shear layer.

The variation of the mean velocity profiles across the cavity are shown in Fig. 20 for $U_\infty = 20$ m/s. The figure shows a comparison of the time-mean development of the shear layer over the cavity, with and without the plasma actuators activated.

The velocity profiles downstream from the leading-edge corner of the cavity exhibit similar mean-flow behavior that characterizes the shear layer and the recirculation region within the cavity. Although

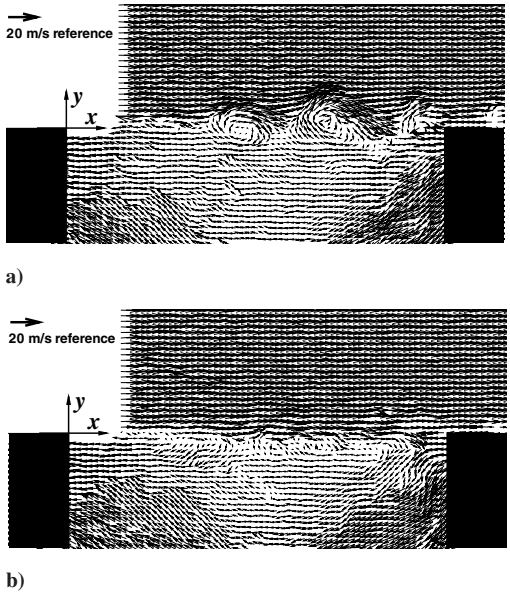

Fig. 19 The intermittence of large vortical structures in the shear layer with plasma actuation visualized using Galilean decomposition: a) large-scale vortices and b) the absence of large-scale vortices; plasma actuators operating at 16.0 $\mathrm{kV_{pp}}$; and $L/D = 1.0$.

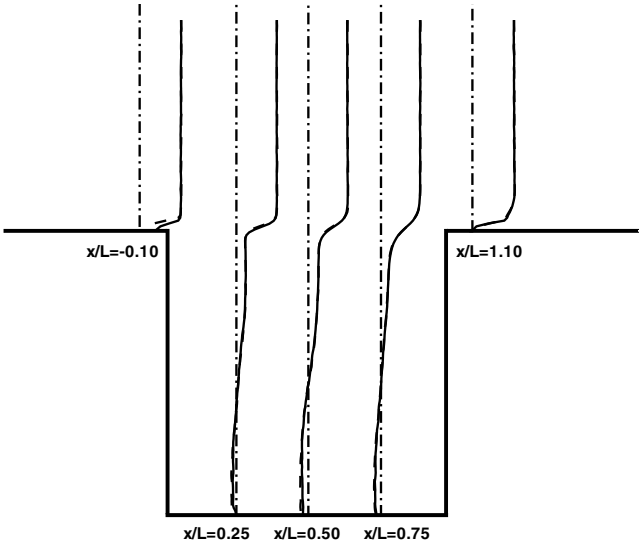

Fig. 20 Streamwise velocity profiles of the time-mean flowfield for $L/D = 1.0$ at $U_\infty = 20$ m/s; actuators active (solid line) and actuators inactive (dashed line).

the plasma actuators have an effect on the time-dependent flowfield, the mean flowfield of the cavity with plasma actuation remains largely the same. To quantify the similarities between the flowfields, the spreading rate of the shear layer, $\mathrm{d}\delta_\Omega/\mathrm{d}x$, was computed from the mean data presented using Eq. (3) [38]. The value of the shear-layer spreading rate is 0.16 for both cases with and without plasma actuation.

$$\delta_\Omega = \frac{u_{\text{upper}} - u_{\text{lower}}}{[d\langle u\rangle/dy]_{\max}} \tag{3}$$

D. Spanwise-Flow Development

The spanwise development of the shear layer was captured by PIV surveys in the $x - z$ plane at $y/D = 0.0$. The plane at $y/D = 0.0$ corresponds to the shear-layer region from the leading-edge corner of the cavity to the trailing-edge corner. The results shown are for $U_\infty = 20$ m/s, but are representative of the data at the lower velocities investigated.

The time-mean spanwise flow for the cavity with $L/D = 1.0$ is shown in Fig. 21. In the figure, the black regions represent the leading- and trailing-edge surfaces of the cavity; the dark gray areas mask data that were corrupted by reflections of laser light from the walls of the cavity saturating the CCD pixels; and the light gray strips represent the location of the plasma actuators and their surrounding glow. The figure shows the spanwise variation in the u velocity for the cases with and without plasma actuation. The effect of the plasma actuators activated produces a spanwise variation in the u velocity field over the cavity.

In Fig. 21a, the flow is dominated by the variation of u velocity in the streamwise direction. The velocity varies from 20 m/s at the leading-edge corner to stagnation at the trailing edge. The increasing proximity of the contour levels downstream from the leading-edge corner indicates a rapid deceleration of the flow at the trailing edge. In Fig. 21b, the effect of the plasma actuators on the spanwise flowfield can be seen. The spanwise variation of the u velocity dominates the flow, showing organized regions of high and low velocity. The observed variation in the flow coincides with the electrode spacing of the actuators and indicates that the upstream disturbances of the plasma actuators convect downstream with the mean flow. The convection of the induced flow by the plasma actuators affects the convection and development of the discrete spanwise vortices in the cavity shear layer. The spanwise variation of the flow over the cavity affects the spanwise coherence of discrete vortices in the cavity shear layer, disrupting the mechanisms that allow the cavity to produce flow-induced tones [39,40]. The high-frequency excitation by the plasma actuators on the flow is not believed to be the mechanism for attenuating the cavity tones, known as the high-frequency excitation (HIFEX) effect [41,42]. It is hypothesized that the high-frequency excitation of the HIFEX effect induces an acceleration of the energy cascade in the inertial subrange, removing energy from the lower flow-induced tonal frequencies [42]. However, the broadband spectrum in Fig. 13 with the plasma actuators activated does not show a change in the low-frequency broadband spectrum, suggesting that the removal of the cavity tone is due to the induced flowfield of the actuators.

The time-mean variation of the w velocity contours is shown in Fig. 22. The w variation in the spanwise flow over the cavity with the plasma actuators activated is shown in Fig. 22b. In the figure, visible columns of w velocity from the leading-edge corner of the cavity to the trailing-edge corner can be observed. The alternating columns of w velocity across the cavity span represent the positive and negative directions of the flow. The spacing of the columns coincide with the electrode arrangement of the plasma actuators, corresponding to the

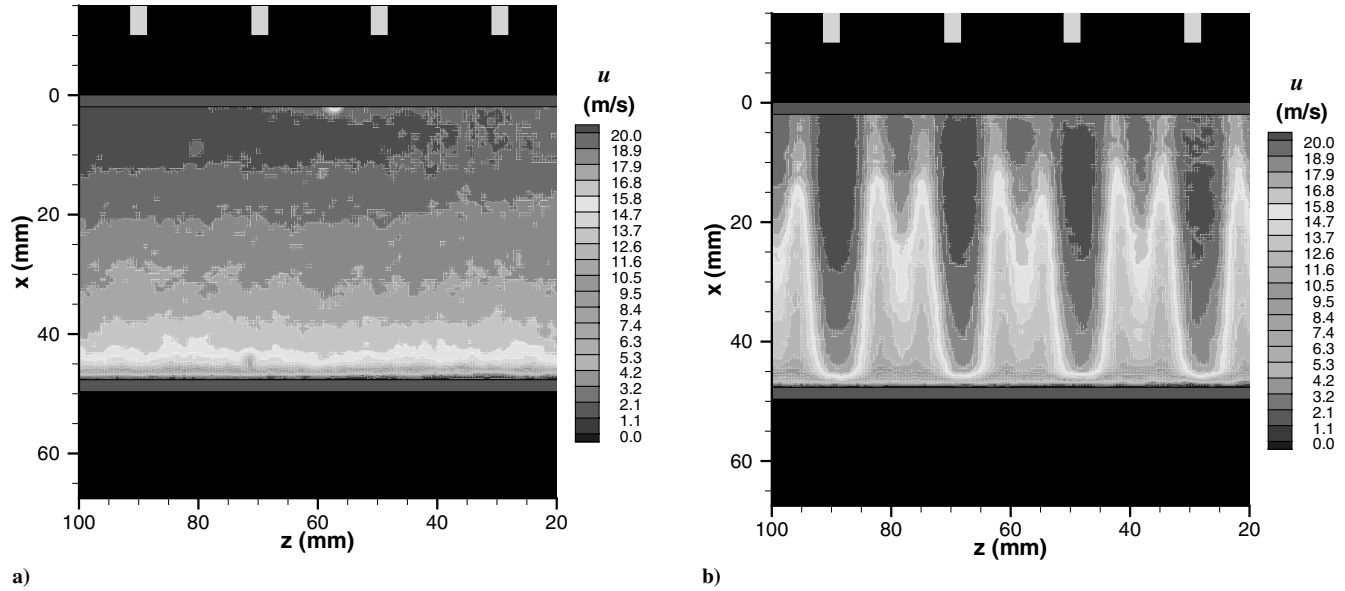

Fig. 21 Contours of $\langle u\rangle$ velocity for a cavity with $L/D = 1.0$ at $U_\infty = 20$ m/s; flow is from top to bottom; and plasma actuators are a) inactive and b) active (16.0 $\mathrm{kV_{pp}}$).

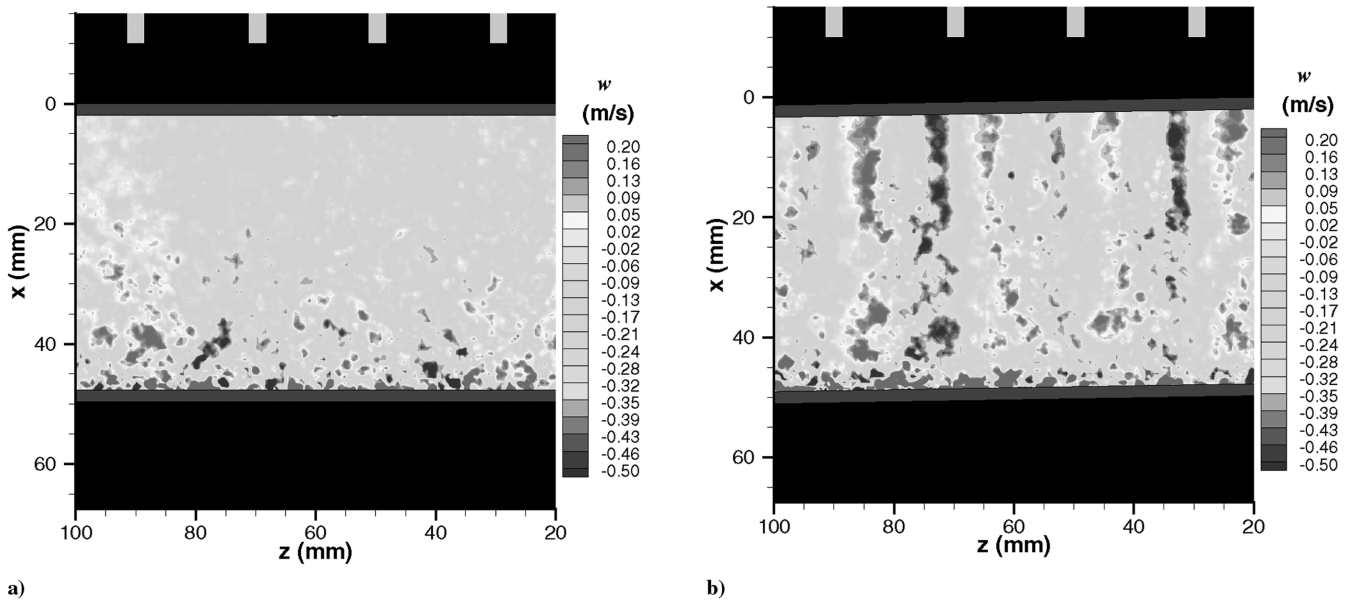

Fig. 22 Contours of $\langle w \rangle$ velocity for a cavity with $L/D = 1.0$ at $U_\infty = 20$ m/s; flow is from top to bottom; and plasma actuators are a) inactive and b) active (16.0 kV_{pp}).

induced streamwise vortices produced upstream by the actuators (Fig. 10). It is likely that the streamwise vortical structures generated by the plasma actuators convect downstream in the boundary layer with the mean flow, and similar results were observed by Zhang [43] using inclined jets. It is surmised that these streamwise vortical structures convect downstream with the mean flow, producing a spanwise variation in the u velocity, shown in Fig. 21b. The variation in the spanwise velocity impedes the development of the coherent spanwise vortical structures that are required for flow-induced cavity tones.

VI. Conclusions

An experimental investigation into the low-subsonic-speed flow around a cavity was performed. The aim of the experimental investigation was to determine the effect of plasma actuators on the acoustic noise radiated from a rectangular cavity. Microphone measurements within the cavity and PIV surveys for a cavity with $L/D = 1.0$ at flow speeds ranging from $U_\infty = 10$ to 20 m/s were conducted. As a result of the investigation, the following points can be made:

1) The dominant cavity mode and its harmonics were attenuated to broadband level when the plasma actuators were activated. The level of attenuation provided by the plasma actuators for a given flow speed was dependent on their operating voltage.

2) The plasma actuators induce fluid motion along the surface of the dielectric, resulting in the formation of streamwise vortical structures between a pair of actuators that convect downstream with the mean flow.

3) The streamwise vortices produce a spanwise variation of the flow over the cavity that impedes the development of the vortices in the cavity shear layer, disrupting the feedback mechanism that is required for self-sustained fluid-dynamic oscillations.

4) Flowfield surveys using PIV show that the plasma actuators affect the instantaneous streamwise flowfield while preserving the mean flowfield. However, the plasma actuators significantly modify the spanwise flow in the shear-layer region of the cavity.

5) High-frequency tones were produced by the plasma actuators, corresponding to the operating frequency of the applied potential. The amplitude of the high-frequency tones increased with the input power, but the rate of increase reduced.

The attenuation of flow-induced tones using plasma actuators was demonstrated. The results show the potential of plasma actuators to aeroacoustic applications and provide a stepping stone for further studies. The work presented in this paper focused on the attenuation of tonal noise produced by the low-speed flow over a cavity. The effect of the plasma actuators on the noise at higher velocities should be investigated to determine the limitations of the current setup. The results also showed the intermittence of vortices in the cavity shear layer when the plasma actuators were activated. Spatial correlations using a hot wire can be used to determine the spatial and temporal intermittence of spanwise vortices in the cavity shear layer. An equally important component of noise is the broadband noise radiation. The successful application of plasma actuators to a similar cavity case study in which the radiated noise is broadband, for example, would potentially lead to a broader range of applications in aeroacoustics. Already, plasma actuators are being investigated to reduce the wake profiles of cylinders and bluff bodies, with the aim of reducing the broadband noise from aircraft landing gear [44,45].

Acknowledgment

Sammie Chan was supported by a studentship from the School of Engineering Sciences, University of Southampton.

References

[1] Crighton., D. G., "Airframe Noise," *Aeroacoustics of Flight Vehicles: Theory and Practice*, NASA RP-1258, Vol. 1, 1991, pp. 391–447.

[2] Macaraeg., M. G., "Fundamental Investigations of Airframe Noise," AIAA Paper 1998-2224, June 1998.

[3] Anon., *Strategic Research Agenda*, Vol. 1, Advisory Council for Aeronautics Research in Europe, Brussels, Belgium, Oct. 2004.

[4] Anon., *Strategic Research Agenda*, Vol. 2, Advisory Council for Aeronautics Research in Europe, Brussels, Belgium, Oct. 2004.

[5] Cattafesta, L. N., Shukla, D., Garg, S., and Ross., J. A., "Development of an Adaptive Weapons-Bay Suppression System," AIAA Paper 1999-1901, May 1999.

[6] Krishnamurty, K., "Acoustic Radiation from Two-Dimensional Rectangular Cutouts in Aerodynamic Surfaces," NACA TN-3487, Aug. 1955.

[7] Roth, J. R., Tsai, P. P., and Liu, C., "Steady-State Glow Discharge Plasma," U.S. Patent 5,387,842, filed Feb. 1995.

[8] Roth., J. R., "Method And Apparatus for Covering Bodies with a Uniform Glow Discharge Plasma and Applications Thereof," U.S. Patent 5,669,583, filed Sept. 1997.

[9] Ráhel, J., and Sherman, D. M., "The Transition from a Filamentary Dielectric Barrier Discharge to a Diffuse Barrier Discharge in Air at Atmospheric Pressure," *Journal of Physics D: Applied Physics*, Vol. 38, No. 4, Feb. 2005, pp. 547–554.

[10] Kogelschatz, U., "Filamentary, Patterned, and Diffuse Barrier Discharge," *IEEE Transactions on Plasma Science*, Vol. 30, No. 4, Aug. 2002, pp. 1400–1408.

[11] Roth, J. R., Sherman, D. M., and Wilkinson, S. P., "Boundary Layer Flow Control with a One Atmosphere Uniform Glow Discharge Surface Plasma," AIAA Paper 1998-0328, Jan. 1998.
[12] Rockwell, D., and Naudascher, E., "Review-Self Sustaining Oscillations of Flow Past Cavities," *Journal of Fluids Engineering*, Vol. 100, June 1978, pp. 152–165.
[13] Rockwell, D., and Naudascher, E., "Self-Sustained Oscillations of Impinging Free Shear Layers," *Annual Review of Fluid Mechanics*, Vol. 11, Jan. 1979, pp. 67–94.
[14] Cattafesta, L. N., III, Williams, D., Rowley, C., and Alvi., F., "Review of Active Control of Flow-Induced Cavity Resonance," AIAA Paper 2003-3567, June 2003.
[15] Rowley, C. W., and Williams, D. R., "Dynamics and Control of High-Reynolds-Number Flow over Open Cavities," *Annual Review of Fluid Mechanics*, Vol. 38, Jan. 2006, pp. 251–276.
[16] Drazin., P. G., *Introduction to Hydrodynamic Stability*, 1st ed., Cambridge Univ. Press, Cambridge, England, U.K., 2002.
[17] Rossiter., J. E., "Wind-Tunnel Experiments on the Flow over Rectangular Cavities at Subsonic and Transonic Speeds," Aeronautical Research Council, Repts. and Memoranda 3438, Oct. 1964.
[18] Cattafesta, L. N., III, Garg, S., Choudhari, M., and Li., F., "Active Control of Flow-Induced Cavity Resonance," AIAA Paper 1997-1084, 1997.
[19] Block., P. J. W., "Noise Response of Cavities of Varying Dimensions at Subsonic Speeds," NASA TN-D-8351, Dec. 1976.
[20] Rockwell., D., "Prediction of Oscillation Frequencies for Unstable Flow Past Cavities," *Journal of Fluids Engineering*, Vol. 99, Dec. 1976, pp. 249–300.
[21] Heller, H. H., Holmes, D. G., and Covert., E. E., "Flow-Induced Pressure Oscillations in Shallow Cavities," *Journal of Sound and Vibration*, Vol. 18, No. 4, 1971, pp. 545–553.
[22] Maina., E. I., "Error and Uncertainty Analysis," *The Development of Passive Flow Control Vortices*, Univ. of Southampton, Southampton, England, U.K., Jan. 2004.
[23] Choi., C. K., "Wind Tunnel Blockage Effects on Aerodynamic Behavior of Bluff Body," *Wind & Structures*, Vol. 1, No. 4, Dec. 1998, pp. 351–364.
[24] Parkinson, G. V., and Cook., N. J., "Blockage Tolerance of a Boundary-Layer Wind Tunnel," *Journal of Wind Engineering and Industrial Aerodynamics*, Vol. 42, Nos. 1–3, Oct. 1992, pp. 873–884.
[25] Roth., J. R., *Industrial Plasma Engineering*, 1st ed., Vol. 2, Inst. of Physics Publishing, Philadelphia, 2001.
[26] Anon., "PIC16F84A Data Sheet," Microchip Technology Inc., Chandler, AZ, 2001.
[27] Corke, T. C., and Matlis., E., "Phased Plasma Arrays for Unsteady Flow Control," AIAA Paper 2000-2323, June 2000.
[28] Shinneeb, A-M., Bugg, J. D., and Balachandar, R., "Variable Threshold Outlier Identification in PIV Data," *Measurement Science and Technology*, Vol. 15, No. 9, July 2004, pp. 1722–1732.
[29] Sarohia., V., "Experimental Investigations of Oscillations in Flows over Shallow Cavities," *AIAA Journal*, Vol. 15, No. 7, Apr. 1997, pp. 984–991.
[30] Moffat., R. J., "Describing the Uncertainties in Experimental Results," *Experimental Thermal and Fluid Science*, Vol. 1, Jan. 1998, pp. 3–17.
[31] Stallings, R. L., and Wilcox, F. J., "Experimental Cavity Pressure Distributions at Supersonic Speeds," NASA TP-2683, June 1987.
[32] Cattafesta, L. N., III, Garg, S., Kegerise, M. A., and Jones, G. S., "Experiments on Compressible Flow-Induced Cavity Oscillations," AIAA Paper 1998-2912, June 1998.
[33] Roth, J. R., Sherman, D. M., and Wilkinson, S. P., "Electrohydrodynamic Flow Control with a Glow-Discharge Surface Plasma," *AIAA Journal*, Vol. 38, No. 7, July 2000, pp. 1166–1172.
[34] Enloe, C. L., McLaughlin, T. E., Van Dyken, R. D., Kachner, K. D., Jumper, E. J., Corke, T. C., Post, M., and Haddad, O., "Mechanisms and Responses of a Dielectric Barrier Plasma Actuator: Geometric Effects," *AIAA Journal*, Vol. 42, No. 3, Mar. 2004, pp. 595–604.
[35] Ethembabaoglu, S., *On the Fluctuating Flow Characteristics in the Vicinity of Gate Slots*, Univ. of Trondheim, Trondheim, Norway, June 1973.
[36] "Plasma Noise in EMI Design," NASA PD-EC-1106, Sep. 1995.
[37] Adrian, R. J., Christensen, K. T., and Liu, Z-C., "Analysis and Interpretation of Instantaneous Turbulent Velocity Fields," *Experiments in Fluids*, Vol. 29, No. 3, Dec. 2000, pp. 275–290.
[38] Geveci, M., Oshkai, P., Rockwell, D., Lin, J. C., and Pollack, M., "Imaging of the Self-Excited Oscillation of Flow Past a Cavity During Generation of a Flow Tone," *Journal of Fluids and Structures*, Vol. 18, No. 6, July 2003, pp. 665–694.
[39] Raman, P., Raghu, S., and Bencic, T. J., "Cavity Resonance Suppression Using Miniature Fluidic Oscillators," AIAA Paper 1999-1900, May 1999.
[40] Arunajatesan, S., Shipman, J. D., Sinha, N., and Seiner, J. M., "Mechanisms in High-Frequency Control of Cavity Flows," AIAA Paper 2003-0005, Jan. 2003.
[41] Ukeiley, L. S., Ponton, M. K., Seiner, J. M., and Jansen, B., "Suppression of Pressure Loads in Cavity Flows," AIAA Paper 2003-181, Jan. 2003.
[42] Stanek, M. J., Raman, G., Kibens, V., Ross, J., Odedra, J., and Peto, J., "Control of Cavity Resonance Through Very High Forcing," AIAA Paper 2000-1905, June 2000.
[43] Zhang, X., "Counter-Rotating Vortices Embedded in a Turbulent Boundary Layer with Inclined Jets," *AIAA Journal*, Vol. 37, No. 10, Oct. 1999, pp. 1277–1284.
[44] Thomas, F., Kozlov, K., and Corke, T. C., "Plasma Actuators for Landing Gear Noise Reduction," AIAA Paper 2005-3010, May 2005.
[45] Asghar, A., and Jumper, E. J., "Phase Synchronization of Vortex Shedding from Two Side-by-Side Circular Cylinders Using Plasma Actuators," AIAA Paper 2004-925, Jan 2004.

A. Tumin
Associate Editor